DTU Library

Upconversion detector for range-resolved DIAL measurement of atmospheric CH$_4$

Meng, Lichun; Fix, Andreas; Wirth, Martin; Høgstedt, Lasse; Tidemand-Lichtenberg, Peter; Pedersen, Christian; Rodrigo, Peter John

Link back to DTU Orbit

Check for updates

Upconversion detector for range-resolved DIAL measurement of atmospheric CH₄

LICHUN MENG,[1,*] ANDREAS FIX,[2] MARTIN WIRTH,[2] LASSE HØGSTEDT,[3] PETER TIDEMAND-LICHTENBERG,[1] CHRISTIAN PEDERSEN,[1] AND PETER JOHN RODRIGO[1]

[1]DTU Fotonik, Department of Photonics Engineering, Technical University of Denmark, Frederiksborgvej 399, 4000 Roskilde, Denmark
[2]DLR (German Aerospace Center), Institute of Atmospheric Physics, 82234 Oberpfaffenhofen, Germany
[3]NLIR ApS, Hirsemarken 1, 3520 Farum, Denmark
*licme@fotonik.dtu.dk

Abstract: We demonstrate a robust, compact, portable and efficient upconversion detector (UCD) for a differential absorption lidar (DIAL) system designed for range-resolved methane (CH₄) atmospheric sensing. The UCD is built on an intracavity pump system that mixes a 1064 nm pump laser with the lidar backscatter signal at 1646 nm in a 25-mm long periodically poled lithium niobate crystal. The upconverted signal at 646 nm is detected by a photomultiplier tube (PMT). The UCD with a noise equivalent power around 127 fW/Hz$^{1/2}$ outperforms a conventional InGaAs based avalanche photodetector when both are used for DIAL measurements. Using the UCD, CH₄ DIAL measurements have been performed yielding differential absorption optical depths with relative errors of less than 11% at ranges between 3 km and 9 km.

References and links

1. T. F. Stocker, D. Qin, G. K. Plattner, M. Tignor, S. K. Allen, J. Boschung, A. Nauels, Y. Xia, V. Bex, and P. M. Midgley, eds., *Climate Change 2013: The Physical Science Basis. Contribution of Working Group I to the Fifth Assessment Report of the Intergovernmental Panel on Climate Change* (Cambridge University, 2014).
2. K. Mach, M. Mastrandrea, T. Bilir, and C. Field, "Understanding and responding to danger from climate change: the role of key risks in the IPCC AR5," Clim. Change **136**(3-4), 427–444 (2016).
3. M. Saunois, R. B. Jackson, P. Bousquet, B. Poulter, and J. G. Canadell, "The growing role of methane in anthropogenic climate change," Environ. Res. Lett. **11**(12), 12 (2016).
4. G. Ehret, C. Kiemle, M. Wirth, A. Amediek, A. Fix, and S. Houweling, "Space-borne remote sensing of CO₂, CH₄, and N₂O by integrated path differential absorption lidar: a sensitivity analysis," Appl. Phys. B **90**(3-4), 593–608 (2008).
5. A. Amediek, G. Ehret, A. Fix, M. Wirth, C. Büdenbender, M. Quatrevalet, C. Kiemle, and C. Gerbig, "CHARM-F-a new airborne integrated-path differential-absorption lidar for carbon dioxide and methane observations: measurement performance and quantification of strong point source emissions," Appl. Opt. **56**(18), 5182–5197 (2017).
6. A. Rogalski, *Infrared Detectors*, 2nd ed. (CRC Press, 2011).
7. H. Riris, K. Numata, S. Li, S. Wu, A. Ramanathan, M. Dawsey, J. Mao, R. Kawa, and J. B. Abshire, "Airborne measurements of atmospheric methane column abundance using a pulsed integrated-path differential absorption lidar," Appl. Opt. **51**(34), 8296–8305 (2012).
8. A. Dumas, J. Rothman, F. Gibert, D. Édouart, G. Lasfargues, C. Cénac, F. L. Mounier, J. Pellegrino, J. P. Zanatta, A. Bardoux, F. Tinto, and P. Flamant, "Evaluation of a HgCdTe e-APD based detector for 2 μm CO₂ DIAL application," Appl. Opt. **56**(27), 7577–7585 (2017).
9. U. N. Singh, T. F. Refaat, S. Ismail, K. J. Davis, S. R. Kawa, R. T. Menzies, and M. Petros, "Feasibility study of a space-based high pulse energy 2 μm CO₂ IPDA lidar," Appl. Opt. **56**(23), 6531–6547 (2017).
10. X. Sun, J. B. Abshire, J. D. Beck, P. Mitra, K. Reiff, and G. Yang, "HgCdTe avalanche photodiode detectors for airborne and spaceborne lidar at infrared wavelengths," Opt. Express **25**(14), 16589–16602 (2017).
11. G. Ehret, P. Bousquet, C. Pierangelo, M. Alpers, B. Millet, J. B. Abshire, H. Bovensmann, J. P. Burrows, F. Chevallier, P. Ciais, C. Crevoisier, A. Fix, P. Flamant, C. Frankenberg, F. Gibert, B. Heim, M. Heimann, S. Houweling, H. W. Hubberten, P. Jöckel, K. Law, A. Löw, J. Marshall, A. Agusti-Panareda, S. Payan, C. Prigent, P. Rairoux, T. Sachs, M. Scholze, and M. Wirth, "MERLIN: A French-German Space lidar Mission Dedicated to Atmospheric Methane," Remote Sens. **9**(10), 1052 (2017).

12. L. Høgstedt, A. Fix, M. Wirth, C. Pedersen, and P. Tidemand-Lichtenberg, "Upconversion-based lidar measurements of atmospheric CO_2," Opt. Express **24**(5), 5152–5161 (2016).
13. V. G. Dmitriev, G. G. Gurzadyan, and D. N. Nikogosyan, *Handbook of Nonlinear Optical Crystals*, 2nd ed. (Springer, 1995).
14. C. L. Tang, "Spontaneous emission in the frequency up-conversion process in nonlinear optics," Phys. Rev. **182**(2), 367–374 (1969).
15. C. R. Phillips, J. S. Pelc, and M. M. Fejer, "Parametric processes in quasi-phasematching gratings with random duty cycle errors," J. Opt. Soc. Am. B **30**(4), 982–993 (2013).
16. J. S. Pelc, L. Ma, C. R. Phillips, Q. Zhang, C. Langrock, O. Slattery, X. Tang, and M. M. Fejer, "Long-wavelength-pumped upconversion single-photon detector at 1550 nm: performance and noise analysis," Opt. Express **19**(22), 21445–21456 (2011).
17. T. Fujii and T. Fukuchi, *Laser Remote Sensing* (CRC Press, 2005).
18. L. Meng, L. Høgstedt, P. Tidemand-Lichtenberg, C. Pedersen, and P. J. Rodrigo, "GHz-bandwidth upconversion detector using a unidirectional ring cavity to reduce multilongitudinal mode pump effects," Opt. Express **25**(13), 14783–14794 (2017).
19. J. S. Pelc, G.-L. Shentu, Q. Zhang, M. M. Fejer, and J. W. Pan, "Up-conversion of optical signals with multi-longitudinal mode pump lasers," Phys. Rev. A **86**(3), 033827 (2012).
20. J. S. Dam, P. Tidemand-Lichtenberg, and C. Pedersen, "Room-temperature mid-infrared single-photon spectral imaging," Nat. Photonics **6**(11), 788–793 (2012).
21. D. Sakaizawa, C. Nagasawa, T. Nagai, M. Abo, Y. Shibata, M. Nakazato, and T. Sakai, "Development of a 1.6 µm differential absorption lidar with a quasi-phase-matching optical parametric oscillator and photon-counting detector for the vertical CO_2 profile," Appl. Opt. **48**(4), 748–757 (2009).
22. F. Gibert, P. H. Flamant, D. Bruneau, and C. Loth, "Two-micrometer heterodyne differential absorption lidar measurements of the atmospheric CO_2 mixing ratio in the boundary layer," Appl. Opt. **45**(18), 4448–4458 (2006).
23. S. Ishii, M. Koyama, P. Baron, H. Iwai, K. Mizutani, T. Itabe, A. Sato, and K. Asai, "Ground-based integrated path coherent differential absorption lidar measurement of CO_2: foothill target return," Atmos. Meas. Tech. **6**(5), 1359–1369 (2013).

1. Introduction

Global warming and climate change are growing threats to our world and pose serious environmental challenges to society [1]. In order to mitigate the effects of climate change, it is important to understand the greenhouse gas (GHG) cycles on a global scale [2]. CH_4, in particular, is the second most relevant anthropogenic GHG after CO_2 and a recent study shows that it plays an increasing role in global warming [3]. Thus, there is a significant interest in developing highly accurate remote sensing systems for CO_2 and CH_4 monitoring.

Two potential and closely related technologies for accurate GHG measurement by means of active remote sensing are the differential absorption lidar (DIAL) and the integrated path differential absorption (IPDA) technique [4, 5]. DIAL can measure the profiles of target gas mixing ratio in a certain range by analyzing the atmospheric backscatter signals on two different wavelengths. In contrast, IPDA does not use backscatter signals from molecules or aerosol but from a hard target. Therefore, IPDA only measures the average mixing ratio of the gas in the columnar volume between transceiver and the hard target. The working principles of these two technologies are nevertheless similar. However, the intensity of the backscatter signal from the hard target is usually much stronger than the one from the atmosphere; therefore, the required detectivity of the detector for the DIAL system should be higher than that for the IPDA system when both systems operate under similar conditions. Unfortunately, the required wavelengths for lidar measurement of the GHGs (CO_2 and CH_4) are within the infrared range, wherein the detectivity of commercially available InGaAs and HgCdTe based infrared detectors are orders magnitude lower than those working in the visible band, i.e. Si based detectors or photomultiplier tubes (PMT) [6]. State-of-the-art airborne and spaceborne lidar applications using direct infrared detectors are currently restricted to deploying IPDA technology [5, 7–11]. The availability of infrared detectors with higher sensitivity will also enable range-resolved DIAL measurements to be performed.

Instead of using direct infrared detectors, a promising approach is to use an upconversion detector (UCD) – a combination of an optical upconverter that efficiently translates infrared signals to the visible region and a visible detector that has high detectivity. Previously, we demonstrated an intracavity UCD for a CO_2 IPDA/DIAL system and compared its

performance against an InGaAs detector [12]. In that UCD, a 20-mm long PPLN bulk crystal was applied to upconvert a 1572 nm signal to 635 nm by mixing with a 1064 nm intracavity pump. Even though our previous UCD did not yet have better performance than the reference InGaAs detector, it showed a high potential for further improvement.

In this paper, we demonstrate an improved upconversion detector which outperforms an InGaAs based avalanche photodetector (APD) for long-range DIAL measurements. A number of improvements over the previous UCD for CO_2 IPDA/DIAL are discussed. This time, the target gas of interest is CH_4 rather than CO_2. We emphasize that this is the first report of a CH_4 lidar enabled by the UCD technology. The on- and off-line signals for probing CH_4 at 1645.55 nm and 1645.86 nm, respectively, are mixed with a 1064 nm pump in a 25-mm long PPLN bulk crystal. The upconverted signal at 646 nm is detected by a standard PMT. The simple and compact receiver optics used with the improved UCD only consists of a 3-inch diameter plano-convex lens with a focal length of 750 mm. The backscatter signals from the atmosphere in ranges of a few kilometers are detected by both our UCD and the conventional InGaAs APD. We experimentally confirm that our UCD achieves better performance thus constituting a novel alternative for atmospheric lidar signal detection.

2. Theory

2.1 Upconversion efficiency and upconverted spontaneous parametric downconversion (USPDC) noise

The upconversion process follows the principle of sum frequency generation. Under the assumption of plane-wave interaction and non-depleted pump used in upconverting the signal, the quantum efficiency (QE) of the upconversion process is given by [13]:

$$\eta_{up} = \frac{P_{up}\lambda_{up}}{P_{IR}\lambda_{IR}} = \frac{32d_{eff}^2 I_p}{\varepsilon_0 c n_p n_{IR} n_{up} \lambda_{up} \lambda_{IR}} L^2 \sin c^2\left(\frac{\Delta kL}{2}\right), \qquad (1)$$

where d_{eff} is the effective nonlinear coefficient of the PPLN crystal, and with subscript $i = up$, IR and p corresponding to the upconverted, infrared signal and pump beams, respectively, P_i is the optical power of each beam, λ_i is the wavelength, n_i is the refractive index, I_p is the pump intensity, L is the length of the PPLN crystal, $\Delta k = |k_{IR} + k_p - k_{up}| - 2\pi/\Lambda$ is the phase mismatch, where Λ is the PPLN poling period and k_i is the wavenumber in the PPLN crystal. In order to achieve optimal upconversion efficiency, the temperature of the crystal should be tuned to ensure $\Delta k = 0$.
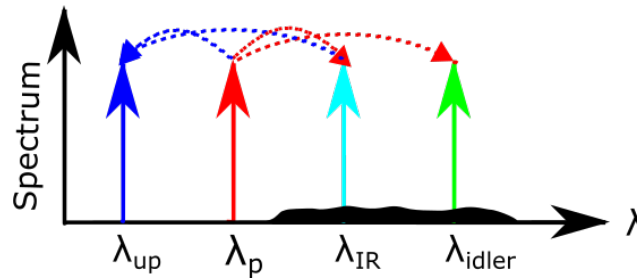

Fig. 1. Illustration of the USPDC process in the PPLN crystal of an upconversion detector. Red dashed arrows represent the spontaneous parametric downconversion of the pump that produces unwanted photons at λ_{IR} and λ_{idler}. Blue dashed arrows denote the upconversion that contributes to the background noise.

One of the main noise sources of our UCD is the upconverted spontaneous parametric downconversion (USPDC) noise [14] and it arises due to presently unavoidable poling error of the nonlinear crystal [15]. Figure 1 illustrates the process of USPDC. The strong pump (λ_p, red arrow) induces a broadband parametric fluorescence (black pedestal) which contains

unwanted signal photons (λ_{IR}, cyan arrow). These unwanted signal photons are spectrally translated (blue dashed arrows) into the same wavelength as the upconverted photons (λ_{up}, blue arrow) and consequently contribute to the background noise in the practical measurement [16].

2.2 Detector étendue

Similar to a conventional detector, the ability of the UCD for infrared signal collection is determined by its étendue ($A\Omega$). A is the detector area and Ω is the solid angle from which the detector can receive the signal. The UCD has a relatively small acceptance angle which is fundamentally limited by the upconversion process [12]. In our experiment, a 25-mm long PPLN is applied, which corresponds to an external acceptance half-angle of 14.7 mrad. The beam waist of the pump inside the PPLN crystal is around 200 µm. Therefore, the étendue of our UCD is $A\Omega$ = 85 µm²rad². On the contrary, the étendue of a typical InGaAs APD for atmospheric lidar application [5] is $A\Omega$ = 2.36 × 10⁴ µm²rad² (diameter D = 0.2 mm; field-of-view (FOV) = 56°), which is around 280 times larger than that of the UCD.

2.3 Signal-to-noise ratio

In our experiments, an InGaAs APD is used as a reference detector to benchmark the performance of our UCD. Meanwhile, the upconverted signal in the UCD is detected by a PMT. For both, APD and PMT, the same formula may be used for signal-to-noise ratio (S/N) calculation [17]:

$$\frac{S}{N} = \frac{i_{signal}}{\sqrt{2eFB\left(i_{signal} + i_b + i_d\right) + i_N^2/M^2}},$$ (2)

where e is the electron charge, B the detection bandwidth, i_{signal} the photocurrent generated by the incident signal photons, i_b the photocurrent due to background noise, i_d the dark current, i_N the amplifier circuit thermal noise, F the noise figure, and M the gain. It has to be emphasized that in comparison to InGaAs APD, the PMT has lower noise figure (F_{APD} » 3; F_{PMT} » 1) and much higher gain ($10 < M_{APD} < 20$; $10^5 < M_{PMT} < 10^6$). Therefore, the PMT generally has better performance in terms of suppressing the noise.

The S/N for the APD can be calculated using Eq. (2) directly. But for the case of the UCD, its quantum efficiency and USPDC noise should be considered along with the properties of the PMT when Eq. (2) is used. The photocurrent of the UCD is:

$$i_{signal} = \frac{P_{IR}\eta_{up}\eta_{PMT}\eta_{opt}e}{\hbar\omega_{IR}},$$ (3)

where ω_{IR} is the angular frequency of the signal, η_{up} and η_{PMT} are the quantum efficiencies for the upconversion and the PMT respectively, while η_{opt} is the coupling efficiency of the optical system. The current due to the background noise is:

$$i_b = \frac{e\left(P_b\eta_{up}\eta_{opt} + AI_{USPDC}\right)\eta_{PMT}}{\hbar\omega_{IR}},$$ (4)

where P_b is the power of the ambient noise, I_{USPDC} is the intensity of the USPDC noise, and A is the cross-sectional area of the pump beam in the PPLN crystal.

In the following experiment, the total quantum efficiency ($\eta_{up}\eta_{PMT}\eta_{opt}$) of the UCD is around 8%, which is smaller than that of the APD (~60%). But the UCD has a higher

detectivity than the APD and it can only succeed in outperforming the APD when relatively weak signals are measured.

3. Characteristics of the UCD

3.1 Setup of the UCD

Figure 2 shows the photo and the schematic diagram of the UCD. Its design is similar to the upconversion module in [18], but some components and parameters are changed in order to suit our CH_4 DIAL application. The poling period of the PPLN crystal is 12.45 µm and the temperature of the crystal is precisely maintained at 129.9 °C (optimal for the chosen combination of on- and off-line DIAL wavelengths) in a temperature controlled oven (Covesion Ltd. PV40 and OC1). The upconverted photons are detected by a PMT (H7422-40, Hamamatsu Photonics) and the PMT output current is amplified by a current amplifier (DHPCA-100, FEMTO GmbH). The output voltage of the current amplifier is treated as the final output of the UCD prior to data sampling (sampled by an A/D converter or monitored by an oscilloscope).
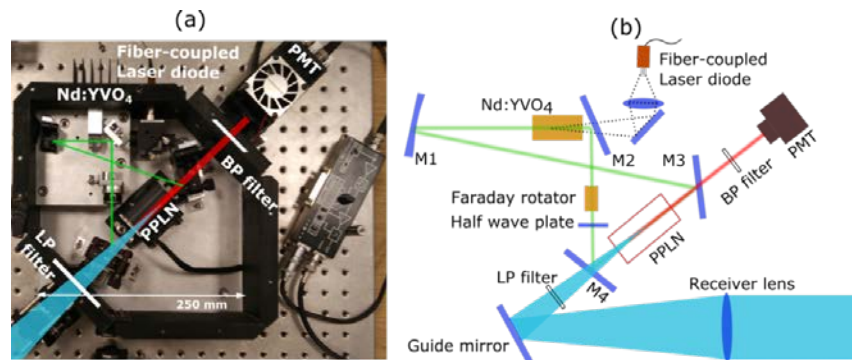

Fig. 2. (a) Top view photo of the UCD. (b) The schematic diagram of the UCD where the guide mirror and the receiver lens are included. M1 is a concave mirror with radius of curvature R = 350 mm, M2 to M4 are plane mirrors, the fiber-coupled laser diode has a core diameter of 200 µm and a NA of 0.22, the PPLN crystal has a length of 25 mm and a poling period of 12.45 µm, the LP filter has a cut-on wavelength of 1250 nm, the BP filter has a central wavelength of 647.1 nm and a bandwidth of 2.5 nm. The cyan, green and red beams represent the 1646 nm signal, 1064 nm pump and 646 nm upconverted signal, respectively.

Based on the experience gained from the preliminary development of our CO_2 lidar UCD [12], the following performance improvements are applied in our new UCD. First, we implement a ring laser cavity with the capability of unidirectional lasing at 1064 nm (upconversion pump wavelength). In comparison to a linear laser cavity used in the CO_2 lidar UCD, the ring design enables single longitudinal mode lasing. At high pump power levels, single mode operation of the ring laser improves upconversion efficiency [19]. Furthermore, unwanted noise due to multimode pumping [18] is avoided. Second, we improve the overall QE of the new UCD by employing a longer PPLN crystal (25 mm versus 20 mm), a larger intracavity pump power (150 W versus 50 W), and a larger pump beam waist w_0 (200 µm versus 100 µm). Third, the étendue of our new UCD is 3.2 times that of the previous one as a result of the combination of larger detection area and slightly reduced acceptance angle (due to longer crystal length). Fourth, more suitable filters are employed in our CH_4 lidar UCD: a long-pass (LP) filter with cut-on wavelength at 1250 nm is placed right before the M4 to filter out the atmospheric stray-light in the visible band; a bandpass (BP) filter (Semrock, LL01-647-12.5) with a central wavelength of 647.1 nm and a bandwidth of 2.5 nm suppresses the pump-induced noise more efficiently. Lastly, a visible PMT with an improved QE (20% versus 8%) is used to detect the upconverted photons at 646 nm. A list of all improvements of the new UCD versus the previously used configuration is given in Table 1.

Table 1. Parameters of our previous and new UCD.

Parameter	UCD in Ref [12].	New UCD
Signal wavelength (nm)	1572	1646
1064 nm pump cavity type	Linear	Ring
Upconverted wavelength (nm)	635	646
PPLN length (mm)	20	25
PPLN period (µm)	11.8	12.45
Intracavity pump power (W)	50	150
Pump beam waist (µm)	100	200
Étendue (µm^{2}rad^2)	25	85
LP filter cut-on wavelength (nm)	n.a.	1250
BW of BP filter, $\Delta\lambda_{up}$ (nm)	10	2.5
Visible PMT Detector	Hamamatsu (R928)	Hamamatsu (H7422-40)
QE of the PMT, η_{PMT}	8% @635 nm	20% @646 nm

3.2 Quantum efficiency of the UCD

In order to optimize the performance of the UCD, the upconversion quantum efficiency is measured as a function of PPLN crystal temperature T. A beam from a cw fiber-coupled DFB laser with a wavelength of 1645.85 nm is focused into the PPLN crystal with precise position and angle tuning for collinear upconversion. Only the unconverted power of the 1646 nm beam through the upconversion module is measured by filtering out all other wavelengths with the LP filter (1250 nm cut-on wavelength) placed in front of a power meter, which temporarily replaces the PMT in Fig. 2(b). The upconversion QE, $\eta_{up}(T)$, is characterized as:

$$\eta_{up}(T) = 1 - P_r(T)/P_R, \tag{5}$$

where $P_r(T)$ is the unconverted 1646 nm power at temperature T. P_R is the transmitted 1646 nm power when no 1064 nm pump is applied.
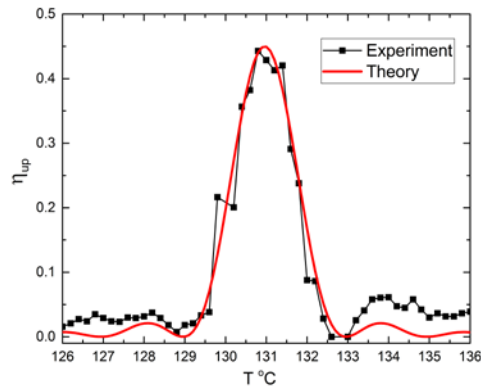

Fig. 3. Measured (black square) and theoretical (red curve) internal quantum efficiency of the upconversion module as a function of temperature of the PPLN crystal. The theoretical curve is horizontally shifted by 2.5 °C so its central lobe coincides with that of the measured points. We attribute the temperature offset to the slight inaccuracy in the refractive indices calculated using the Sellmeier equation.

Figure 3 shows the relation between the internal upconversion efficiency (i.e. without the effect of transmission losses due to cavity mirrors) and the temperature of the PPLN crystal. At a signal wavelength of 1645.85 nm, the UCD achieves maximum internal QE of 45% at a PPLN crystal temperature around 131 °C. During long-term operation, the temperature was stabilized to better than 0.02 °C, thus, variations in the QE of the UCD due to temperature changes can be neglected.

The intracavity pump power is monitored by measuring the proportional 1064 nm leakage power through M1 [see Fig. 2(b)]. Over a 30-minute period, the measured 1064 nm leakage power is 16.4 ± 0.2 mW (sampled every 3 minutes). Therefore, the standard deviation in the UCD quantum efficiency caused by pump power variation is only around 1.2% during half an hour period. In a calibration measurement, we found that 16.4 mW leakage power corresponds to ~150 W intracavity pump power.

3.3 Noise properties of the UCD

Our UCD can be treated as a combination of an upconversion module and a PMT. The *S/N* of the UCD can be calculated using Eq. (2) by considering the following two prevailing optical noise sources, which potentially contribute to the background noise current i_b.

• The atmospheric background noise at 1646 nm.

A long-pass filter with a cut-on wavelength at 1250 nm is applied in front of the entrance of the UCD to block the solar background noise that the PMT is sensitive to. The PPLN crystal has a small acceptance bandwidth (~0.6 nm) and a small acceptance angle (< 20 mrad) for the input 1646 nm signal. Thus, the upconversion process acts as both a spectral and a spatial filter that suppresses the atmospheric noise further. In general, the atmospheric background noise at 1646 nm is negligible in comparison to other noise sources in our UCD.

• Noise generated in the upconversion process.

Upconverted thermal noise [20], upconverted Raman scattering noise [16] and the USPDC noise are the inherent noise sources in the upconversion module. The bandpass filter in front of the PMT can filter the broadband noise (upconverted thermal and upconverted Raman scattering noise) efficiently. However, it is not possible to remove the USPDC noise completely due to its spectral overlap with the upconverted signal.

In order to quantify the noise generated by the current amplifier, the PMT, and the upconversion module, the output of the current amplifier is monitored by an oscilloscope under three conditions: (i) only the output voltage of the current amplifier (N_{AMP}), (ii) the combination of the current amplifier and the PMT ($N_{AMP + PMT}$), and (iii) the overall output of the UCD (at 150 W circulating pump power) without infrared signal input ($N = N_{AMP + PMT + UP}$). The output signal is sampled over 2 ms at a rate of 25 MHz. The measured root mean squares (RMS) of the sampled output voltage values are listed in Table 2. The comparison of the RMS values shows that the dominant noise originates from the upconversion module.

Table 2. Noise in different parts of the upconversion detector system.

Noise source	N_{AMP}	$N_{AMP + PMT}$	$N = N_{AMP + PMT + UP}$
RMS (mV)	2.3	73	179

Considering the internal upconversion efficiency η_{up} (45%), the estimated optical coupling efficiency η_{opt} (85%), the PMT sensitivity S (106 mA/W) at 646 nm, the PMT gain M (1.1 × 10^5), the transimpedance R_f (10^5 V/A) of the current amplifier and its detection bandwidth B (10 MHz), the noise equivalent power (NEP) of the UCD is estimated to be around 127 fW/Hz$^{1/2}$ using Eq. (6):

$$\text{NEP} = \frac{N}{\eta_{up}\eta_{opt}SR_f M \sqrt{B}}. \tag{6}$$

4. Experiment

4.1 IPDA measurement

In order to evaluate the improvement of the new UCD over the previous one, the new UCD is tested under similar conditions as the experiment described in [12] using the CHARM-F system [5] designed as an airborne lidar demonstrator for the French/German MERLIN mission [11]. CHARM-F was devised to measure both CO_2 and CH_4. While in the preceding study [12] the CO_2 channel was used, here we employed the CH_4 channel, only. The return signal from a hard target (i.e. the forest located 2.3 km away from the laboratory building) is simultaneously measured by the InGaAs PIN detector of CHARM-F and the UCD. CHARM-F operates in a double pulse mode with a repetition rate of 50 Hz. The wavelengths of the two pulses are 1645.56 nm and 1645.84 nm, which correspond to the on- and off-line of the chosen resonance frequency of the CH_4 molecule. The pulse duration is 20 ns and the pulse energy is around 10 mJ. CHARM-F has two receiver systems. One consists of a 200-mm diameter Cassegrain telescope and a 1-mm InGaAs PIN detector; the other, of a 60-mm diameter lens with a 0.2-mm InGaAs APD detector. More specific information about CHARM-F can be found in [5]. As a deviation from the parameters described in [5] the divergence of the transmit beam was reduced from ~3 mrad (chosen to optimize IPDA measurements from aircraft) to ~0.9 mrad which is much better adapted to the FOV of the UCD. In our previous work on CO_2 lidar measurements with a UCD, an 8-f scaling system with a demagnification of 250 was applied to collimate the backscatter signal into the PPLN crystal. In contrast, the present infrared signal is focused into the PPLN crystal by a single 3-inch diameter plano-convex lens. Figure 4 shows a sketch of the experiment setup.
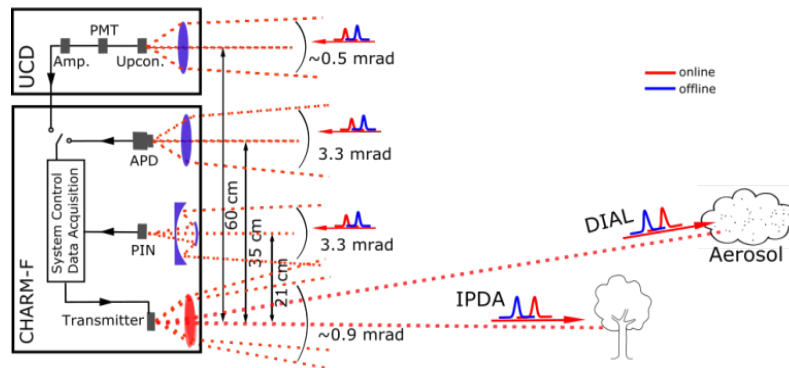

Fig. 4. Conceptual sketch of the setup used for the lidar measurements. For comparison with CHARM-F detectors, the UCD can be connected to the data acquisition card otherwise used to digitize the APD signal. For the IPDA measurement the beam was directed to a distant forest. For the DIAL measurements the entire system was tilted such that the beam propagated beyond the tree tops. For mechanical reasons, the lateral distance between outgoing beam and detector is larger for the UCD in comparison to the CHARM-F receivers. The divergence angle of the transmitter and the receivers' FOVs are also given (not drawn to scale).

Figure 5 shows the normalized backscatter signal measured by the UCD and the PIN detector. The relative absorption as measured by the PIN is of the order of 0.7 which is what is expected from an average CH_4 mixing ratio of ~1.9 ppmv (using HITRAN 2012). For energy referencing, the internal calibration chain of CHARM-F was used where the ratio of the outgoing on- and off-line pulses are measured by the same PIN. This was, however, not possible with the UCD. Therefore, the energies were referenced to the energy ratio measured

by the PIN. Due to the slightly lower conversion efficiency of the UCD at the on-line wavelength at the selected crystal temperature which was confirmed by lab measurements, the ratio of the on- to off-line return signals is somewhat lower.

The signals at ~18 km range depicted in the inset of Fig. 5 show the background noise. The root mean square (RMS) of the background noise given by the UCD is only 1.3 times that of the PIN detector. On the contrary, the RMS given by the previous UCD was ~3.5 times larger than that of the PIN detector [12]. Moreover, benefiting from the improvement of the new UCD, the peak power of the upconversion signal from a hard target can easily saturate the PMT when the recommended gain (10^5 to 10^6) is applied. The gain setting for the UCD data in Fig. 5 is only around 10^3, which implies that our UCD is expected to perform even better if a signal with lower intensity (e.g. atmospheric backscatter signal) is measured and a higher PMT gain setting is used. The result given by the UCD during the IPDA measurement indicates that our UCD can even detect much weaker signals using an appropriate PMT gain. In order to fully explore the potential of the UCD, the atmospheric backscatter signal (few orders of magnitude lower than the IPDA hard target signal) was measured, enabling real DIAL measurements.
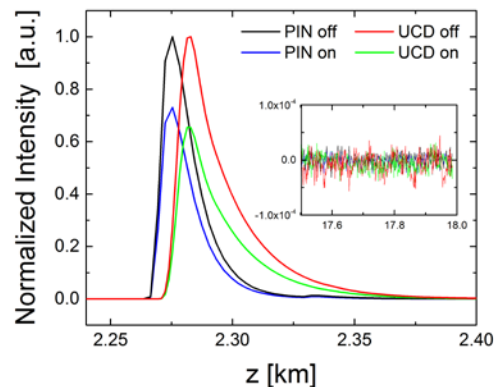

Fig. 5. Backscatter signal from the forest located 2.3 km away measured by the UCD and the reference InGaAs PIN detector and the background signal (inset) from a range of 17.5 km and beyond. The plots are the averages over 6000 pulse pairs (i.e. averaging time of 2 minutes).

4.2 DIAL measurement

First CH_4 DIAL measurements were performed in Oberpfaffenhofen, Germany on June 23rd, 2017 around 11 a.m. UT. The weather was mostly sunny, with few clouds. The temperature was ~27 °C and weak (~4 m/s) westerly winds prevailed. The lidar transceiver was slant-pointed at ~6° out of the laboratory window steering over the forest such that no hard target (e.g. trees) remained in the beam path. The InGaAs APD in the CHARM-F has better performance than the PIN detector when the atmospheric backscatter signal is measured. Therefore, it is the APD instead of the PIN detector that is used as a reference for comparison with the UCD measurement. Since APD and UCD-PMT require the use of the same data acquisition card they cannot operate simultaneously. Therefore, UCD and APD are sequentially applied for the DIAL measurements with each measurement lasting 15 minutes. The separation between the two measurements was around 40 minutes. The data was digitized at a sampling rate of 100 MHz for both measurements.

The divergence angle of the transmitter is ~0.9 mrad. The nominal FOV of the APD based receiver is 3.3 mrad. The lateral distance between APD and transmitter beam is 35 cm while it is larger (60 cm) between UCD and transmitter beam due to mechanical constraints (see Fig. 4). Therefore the full overlap between transmitter and UCD is shifted towards longer distances. The FOV of the UCD based receiver can be estimated as 0.5 mrad given the ratio between pump diameter (400 µm) and receiver lens focal length (750 mm).

In analogy to the data presented in [21], Fig. 6(a) shows range-corrected backscatter signal given by the APD and the UCD at position z upon averaging echoes from 45000 pulse pairs (corresponding to a 15-minute average). Due to the stronger on-line absorption by the CH_4 in the atmosphere, the ratio of the off- to the on-line signal becomes larger with increasing distance. In order to compare the performance of the APD and the UCD, ratios of the raw on-line signal average $<P>$ to its standard deviation σ_P measured by both detectors are shown in Fig. 6(b).
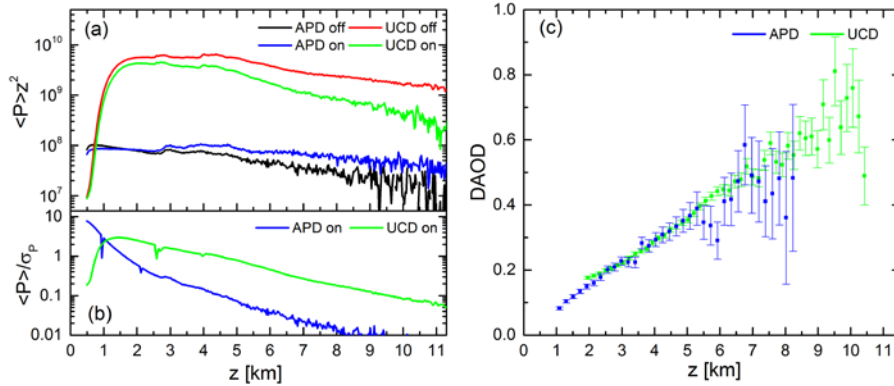

Fig. 6. (a) Range dependence of the on- and off-line range-corrected signals given by the APD and the UCD, (b) signal-to-noise ratio of the on-line backscatter measurement, and (c) the DAOD given by the two detectors. All results are obtained by averaging 45000 pulse pairs (averaging over 15 minutes).

Based on the NEP of the UCD and the bandwidth of the detection, the noise floor of the UCD can be calculated as 0.4 nW, which corresponds to the intensity of the on-line signal at a range of 5.2 km. For the APD, the NEP can be calculated as 240 $fW/Hz^{1/2}$ by considering the RMS of the APD signal at around 18 km (1.36 nA), the APD sensitivity at 1646 nm (1.8 A/W) and the detection bandwidth B (10 MHz). The noise floor is in the 0.8 nW level, and the S/N for the on-line signal is unity at a range of 1.5 km, already. For $z > 3$ km, the $<P>/\sigma_P$ of the UCD is more than 5 times better than that of the APD and it clearly shows that the UCD outperforms the APD for this DIAL measurement. In order to obtain the same statistical error when using the UCD, the averaging time thus can be reduced by more than an order of magnitude.

Based on the on- and off-line signal given by the detectors, the differential absorption optical depth (DAOD) and its corresponding error bars are shown in Fig. 6(c). Similar to the method used in [22, 23], the DAOD is calculated using Eq. (7):

$$\text{DAOD}(z) = \frac{1}{2}\ln\left[\frac{P^{off}(z)P^{on}_{pulse}}{P^{on}(z)P^{off}_{pulse}}\right], \tag{7}$$

where $P^{on,off}(z)$ is the backscatter signal measured by the detector and $P^{on,off}_{pulse}$ is the reference pulse energy. The DAOD of the UCD in Fig. 6(c) increases linearly at ranges between 3 km and 9 km with relative errors from 3% to 11%. The DAOD of the APD that was recorded ~40 minutes later shows the same range dependence although, as expected, with much higher error bars.

The range-resolved CH_4 mixing ratio can be obtained based on the data in Fig. 6(c) using the temperature and pressure dependent absorption cross sections of the CH_4 molecule with respect to the on- and off-line wavelengths. The slopes in Fig. 6(c) suggest a rather constant CH_4 mixing ratio of ~1.9 ppmv in the boundary layer. However, since the angle of inclination of our transceiver was not very accurately calibrated and no means for intercomparison of the

methane mixing ratio was available during this preliminary experiment we refrain from deriving the range-resolved mixing ratio at this stage.

5. Discussion

Our previous UCD showed great potential for IPDA CO_2 detection even though its relatively low QE and small étendue limited its performance [12]. In our new CH_4 lidar UCD, these two parameters are effectively improved by applying altogether a ring cavity, a higher pump power, a larger pump area, a longer PPLN crystal, and a visible PMT with improved QE (see Table 1). Due to these improvements, our new UCD outperforms the InGaAs APD detector when used for CH_4 lidar applications.

In our previous CO_2 measurement, an 8-inch diameter Cassegrain telescope [12] was used for the infrared signal collection. Due to the relatively small étendue of the upconversion module, only a small part of all infrared photons collected by the telescope were upconverted. Furthermore, the secondary mirror of the Cassegrain telescope presumably blocked a part of the infrared signal. In our new UCD receiver system, only a single 3-inch diameter plano-convex lens with a focal length of 750 mm was used. The simple receiver lens system makes the signal collection more efficient and easier to adjust. As before, the CHARM-F system [5] was used as the testbed to compare the UCD receiver to the existing state-of-the-art.

Already at moderate gains of the PMT in the UCD, the backscatter signal from a hard target (2.3 km away) became saturated in our IPDA measurement which could be avoided by either attenuating the energy of the transmitted (or received) pulses or by selecting a hard target at a much farther range (>10 km). The data in Fig. 5 shows that the detection efficiency of the UCD for the off-line signal was ~14% higher than that for the on-line. In future IPDA measurements, therefore, the relative detection efficiency of the UCD should be calibrated before performing columnar average CH_4 mixing ratio calculation. No calibration, however, is required for the DIAL technique and the high sensitivity of the UCD versus direct detectors make such measurements possible resulting in range-resolved lidar measurements.

The DIAL measurement results shown in Fig. 6 demonstrate that the UCD outperforms the InGaAs APD. Although the more direct *S/N* comparison of the two detectors in Fig. 5 shows comparable performance, we emphasize that the PMT gain setting used for the UCD in our IPDA measurement was relatively low (i.e. 10^3) to avoid saturation. In the DIAL experiment where the lidar system was pointed away from the hard target, it was possible to increase the PMT gain to 10^5, thereby increasing the *S/N* performance of the UCD and allowing for range-resolved CH_4 DIAL measurements.

Our UCD can easily be extended to other gas-sensing lidar applications working in the mid-infrared region (e.g. 2 µm to 5 µm) by simply changing the PPLN poling period, spectral filters, and a cavity mirror [M4 in Fig. 2(b)] to match the specific mid-infrared signal wavelength. Due to high detectivity and room-temperature operating condition, the mid-infrared UCD can serve as better alternative to conventional mid-infrared detectors (e.g. cryogenically cooled HgCdTe or InSb detector) in atmospheric lidar applications.

6. Summary

In this work, the first IPDA and DIAL measurements of CH_4 using an upconversion-based detector is demonstrated. Benefiting from the high signal-to-noise ratio performance of an improved upconversion detector, our system possesses the ability to measure the DAOD between 3 and 9 km with relative errors smaller than 11%. Our CH_4 lidar UCD outperforms a conventional InGaAs APD detector and shows a strong potential as an alternative detector for future DIAL applications in wavelength ranges where direct detectors have limited performance and where high quantum efficiency and low noise are required.

Funding